Volume 6
Number 5
7 February 2018
Pages 911-1266

Journal of
Materials Chemistry C

Materials for optical, magnetic and electronic devices

rsc.li/materials-c

ISSN 2050-7526

ROYAL SOCIETY
OF CHEMISTRY

PAPER
Nosang V. Myung, Yong-Ho Choe *et al.*
A noble gas sensor platform: linear dense assemblies of
single-walled carbon nanotubes (LACNTs) in a multi-layered
ceramic/metal electrode system (MLES)

This is an Accepted Manuscript, which has been through the Royal Society of Chemistry peer review process and has been accepted for publication.

Accepted Manuscripts are published online shortly after acceptance, before technical editing, formatting and proof reading. Using this free service, authors can make their results available to the community, in citable form, before we publish the edited article. We will replace this Accepted Manuscript with the edited and formatted Advance Article as soon as it is available.

You can find more information about Accepted Manuscripts in the Information for Authors.

Please note that technical editing may introduce minor changes to the text and/or graphics, which may alter content. The journal's standard Terms & Conditions and the Ethical guidelines still apply. In no event shall the Royal Society of Chemistry be held responsible for any errors or omissions in this Accepted Manuscript or any consequences arising from the use of any information it contains.

ROYAL SOCIETY
OF CHEMISTRY

rsc.li/materials-c

Persistent Luminescence of Transparent ZnGa$_2$O$_4$:Cr^{3+} Thin Films from Colloidal Nanoparticles of Tunable Size

Encarnación Arroyo, Beatriz Medrán, Victor Castaing, Gabriel Lozano,* Manuel Ocaña, Ana I. Becerro*

Instituto de Ciencia de Materiales de Sevilla (CSIC-US), c/Américo Vespucio, 49. 41092 Sevilla, Spain

Journal of Materials Chemistry C Accepted Manuscript

* Corresponding authors: anieto@icmse.csic.es (A.I.B.) and glozano@icmse.csic.es (G.L.)

ABSTRACT: We report on the fabrication of $ZnGa_2O_4$:Cr^{3+} transparent thin films and the evaluation, for the first time in literature, of their persistent red to NIR emission. For this purpose, we have used a simple and economic global strategy based on wet processing methods from colloidal nanospheres with uniform size. A microwave-assisted hydrothermal method was first developed for the synthesis of the precursor particles, which allows size tuning from 300 nm to 30 nm through simple modification of the Zn precursor and the Cr content of the starting solutions. $ZnGa_2O_4$:Cr^{3+} transparent thin films over quartz substrates were then easily fabricated by spin coating, and their structural and optical characteristics were analyzed in detail after annealing at high temperature to elucidate the effect of processing temperature and particle size on films properties. Indeed, our results indicate that high temperature annealing does not compromise the transparency of the films while improves their photoluminescence. In addition, the analysis reveals that persistence luminescence in our films is rather independent of the size of the precursor nanoparticles. Due to their transparency and persistent emission properties, films fabricated from colloidal suspensions of $ZnGa_2O_4$:Cr^{3+} nanoparticles show great potential for applications in the fields of chemical sensing, information storage, labelling, and anti-counterfeiting technology.

Journal of Materials Chemistry C Accepted Manuscript

1. Introduction

Persistent luminescence is a phenomenon where a material can still emit light long after the exciting source (ultraviolet light, X-rays, electrons or even gamma radiation) has been removed. The inorganic materials showing "persistent luminescence" are referred to as "persistent phosphors" while the term "phosphorescence" is reserved to refer to this phenomenon in organic molecules.[1] Persistent phosphors can store excitation energy in intrinsic traps in the form of holes or electrons and further release the trapped charges to give rise to the emission of photons under thermal or physical stimulation.[2] Persistent luminescence materials have a wide range of application in the fields of bioimaging,[3] chemical sensing,[4] information storage,[5] signaling,[6] or anti-counterfeiting technology.[7]

The use of persistent luminescence materials for many of the mentioned applications demands their preparation in the form of transparent thin films, rather than simply employing the pristine powders or using them in the form of nanoparticles. In this context, films of phosphorescence organic materials such as polymers,[8] metal-organic frameworks[9] and carbon dots[10] have been reported. However, they typically suffer from low thermal and chemical stability, which precludes their use in most applications. To overcome these drawbacks, films based on persistent phosphors (mainly green emitting $SrAl_2O_4$:Eu^{2+},Dy^{3+}) have been also reported.[11,12,13,14,15]

Chromium doped zinc gallate ($ZnGa_2O_4$:Cr) is another persistent phosphor with emission located in the red to near infrared (NIR) region. Zinc gallate shows cubic spinel structure. The Ga^{3+} ion occupies the octahedral sites (B sites), and the Zn^{2+} ions occupy the tetrahedral sites (A sites). It exhibits a slight inversion character, wherein a few percent (~3%) of Zn^{2+} occupies the B sites (called Zn_{Ga}' defect) while the same percentage of Ga^{3+} occupies the A sites (called Ga_{Zn}° defect). Such defects in the host matrix are called antisite defects. The persistent emission of $ZnGa_2O_4$:Cr originates on the Cr ions possessing a neighboring antisite defect pair after excitation with the suitable wavelength. The excitation energy is stored in such defects that act as intrinsic traps. Further thermal stimulation gives rise to the emission of red to NIR photons.[16,17,18] Because of this property, $ZnGaO_4$:Cr persistent nanoparticles and bulk phosphors powders have been widely studied recently.[16,17,19,20,21,22,23]

Although several studies have been published about the fabrication of $ZnGa_2O_4$:Cr thin films,[24,25,26,27] none of them mention their persistent luminescence and, consequently, no

study about the persistent luminescent properties of $ZnGa_2O_4$:Cr thin films has been reported up to now. Persistent thin films made out of $ZnGa_2O_4$:Cr are attractive as nano-sized sensing displays with potential applications in anti-counterfeiting technology. From the academic point of view, such nanodevices would also be interesting to show the influence of annealing conditions and nanoparticles size on the persistent luminescence properties of nanophosphors. These persistent nanophosphor films studies would be complementary to previous studies that have been carried out on nanoparticles powders[21,22,28] and on nanoparticles embedded in transparent media such as nano glass-ceramics.[29,30]

Most of the reported $ZnGa_2O_4$:Cr films were prepared by magnetron sputtering[25,26] or laser ablation,[27] which result expensive and complex techniques. It is well-known that spin coating starting from a suspension of precursor nanoparticles (NPs) is an interesting alternative to obtain transparent thin films with controlled thickness, which is simpler and more economical.[31] Therefore, the preparation of $ZnGa_2O_4$:Cr transparent films by spin coating from NPs suspensions would be of high interest. It is necessary that the precursor material be a colloidal suspension of uniform nanoparticles of small size to avoid light scattering. $ZnGa_2O_4$:Cr NPs have been typically synthesized, with bioimaging purposes, following a hydrothermal method in autoclave. Such an approach is time- and energy-consuming, as it needs reaction times of 10 h to 20 h and temperatures of ~200 ºC.[32,33,34,35] Teston et al.[36] reported a singular method based on the use of benzyl alcohol and microwave assisted heating at 270 ºC for 30 minutes. Although, it renders ultrasmall $ZnGa_2O_4$:Cr nanoparticles with a considerable reduction of reaction time, the method presents severe limitations to yield uniform particles of controlled size. A different synthesis method also using microwaves heating was also reported by Sun et al.,[37] who also obtained heterogeneous particles. Therefore, an alternative synthesis method that renders uniform, well-dispersed $ZnGa_2O_4$:Cr NPs of tunable size is demanded. The resulting NPs could then be used to easily fabricate transparent thin films and analyze the influence of particle size on their persistent luminescence.

In this work, we first develop a facile synthesis method that renders highly monodisperse $ZnGa_2O_4$:Cr spheres (Cr = 0 to 1 mol %) with tunable diameter in a large interval (300 nm to 30 nm). The method consists in aging, at 200 ºC for 30 minutes, an aqueous solution of Zn nitrate (or Zn acetate), Ga nitrate, Cr nitrate and trisodium citrate in a microwave oven. The particle size can be modulated by using either Zn nitrate or Zn acetate as the

Zn source and by varying the Cr^{3+} content of the starting solution. Secondly, we demonstrate that highly transparent, $ZnGa_2O_4$:Cr thin films of uniform thickness can be prepared by spin coating using either the smallest or the largest particles obtained as above within the nanometer range (30 nm and 100 nm). Finally, a comparative study of the optical and photoluminescent properties of these films, including persistent luminescence and thermally stimulated luminescence, is carried out to evaluate the influence of particle size on such properties. This is, to the best of our knowledge, the first report about the persistent luminescent properties of transparent $ZnGa_2O_4$:Cr thin films.

2. Experimental section

2.1. Materials

2.1.1. Chemicals

Zinc nitrate hexahydrate ($Zn(NO_3)_2 \cdot 6H_2O$, Sigma Aldrich, 99.99%), zinc acetate ($Zn(OAc)_2$, Sigma Aldrich, 99.99%), gallium nitrate hydrate ($Ga(NO_3)_3 \cdot xH_2O$, Sigma Aldrich, 99.9%), chromium nitrate nonahydrate ($Cr(NO_3)_3 \cdot 9H_2O$, Sigma Aldrich, 99%), trisodium citrate dihydrate ($HOC(CO_2Na)(CH_2CO_2Na)_2 \cdot 2H_2O$, Sigma Aldrich, 99.5%), tetraethylammonium hydroxide ($C_8H_{21}NO$, TEAH, Fluka), zirconium (IV) n-propoxide 70% in 1-propanol (Aldrich), triblock copolymer Pluronic F127 (Mw ≈ 12 600), 2,4-Pentanedione (acetylacetonate, AlfaAesar), HCl (37%, Sigma Aldrich) and MilliQ water were used without further purification (or as received).

2.1.2. Synthesis of $ZnGa_2O_4$:Cr nanoparticles

The $ZnGa_2O_4$:Cr particles were obtained using the hydrothermal method. Two series of samples were synthesized which just differed in the salt used as Zn precursor (nitrate or acetate) with nominal Cr contents from 0 to 20 mol % relative to $ZnGa_2O_4$. The synthesis of the undoped particles was carried out by mixing aqueous solutions of $Zn(NO_3)_2$ or $Zn(OAc)_2$ (15 mL, 0.04 M), $Ga(NO_3)_3$ (15 mL, 0.08M) and sodium citrate (30 mL, 0.1 M) with magnetic stirring at room temperature for 30 minutes. After homogenization, TEAH was added to the solution until pH=9. After additional stirring for 15 minutes, the solution was transferred to a tightly close reactor and heated at 200 ºC, with a heating rate of 14 °C min⁻¹, for 30 minutes in a microwave oven (Sineo MDS-8). The resulting

dispersion was cooled down to room temperature and washed three times with distilled water. The aqueous suspension was dried at 60ºC for some analyses.

The Cr-containing nanoparticles were synthesized by adding stoichiometric amounts of $Cr(NO_3)_3$ to the starting aqueous solution of the Ga salt, and following identical procedure as for the undoped particles described above.

Samples synthesized from Zn acetate and Zn nitrate will be called AZG-x and NZG-x, respectively, where x is the nominal Cr content in $ZnGa_2O_4$:Cr expressed in mol % relative to Zn.

2.1.3. Preparation of $ZnGa_2O_4$:Cr thin films

Preparation of thin films is schematized in Figure 1. The AZG-12 and NZG-20 nanoparticles synthesized as above were deposited on quartz substrates by spin coating to fabricate uniform thin films. The adhesiveness of the nanoparticles to the quartz was improved by the deposition of a ZrO_2 thin layer between the quartz and the nanoparticles. We have experimentally observed that such thin layer not only improves the adhesiveness but also the uniformity of the nanophosphor films deposited atop, which may originate from the different surface charge of the ZrO_2 film compared to the quartz substrate. [38]
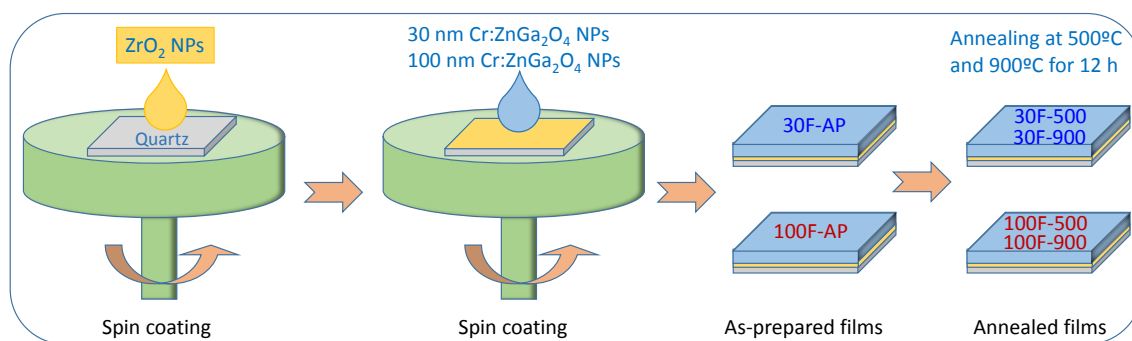

Figure 1: Synthesis of $ZnGa_2O_4$:Cr^{3+} thin films by spin coating on quartz substrates. A thin layer of ZrO_2 nanoparticles is deposited first to improve the adhesiveness of the $ZnGa_2O_4$:Cr^{3+} nanoparticles to the quartz.

The ZrO_2 film was deposited over the quartz substrate using a ZrO_2 precursor sol prepared using the method reported by Zelcer et al.[39] Briefly, the ZrO_2 sol was prepared by mixing ethanol, acetylacetonate, zirconium n-propoxide, HCl, water and F127 in a 40:1:1:1:20:0.005 molar ratio. Zirconium propoxide, acetylacetonate, and F127 were dissolved in 80% of the total ethanol and the mixture was stirred for 1 min. HCl and water dissolved in the remaining ethanol were added dropwise while stirring to the first solution, which was further stirred for 1 h. A total volume of 160 μL of the thus prepared ZrO_2 sol

was spin coated (Laurell WS-400) on the quartz substrate (25 mm x 25 mm) with an acceleration ramp of 11340 rpms^{-1} and a final rotation speed of 3000 rpm. The film was then annealed at 300 °C for 30 min.

Two $ZnGa_2O_4$:Cr thin films were then deposited over the quartz/ZrO_2 substrates by spin coating using 180 μL of AZG-12 or NZG-20 nanoparticles dispersed in methanol (30 mg NPs/mL) with a rotation speed of 1500 rpm. The spin coating process was repeated 3 times for the AZG-12 nanoparticles and twice for the NZG-20 ones. The films were then annealed at 500 ºC and 900 ºC for 12 hours at 1 ºC·min^{-1}. The films prepared from the AZG-12 and NZG-20 will be named 30F and 100F, respectively, because the diameter of the corresponding nanoparticles were 30 nm and 100 nm, as described below.

2.2. Characterization techniques

2.2.1. Structural characterization of the $ZnGa_2O_4$:Cr^{3+} particles and films

Transmission electron microscopy (TEM, JEOL2100Plus) was used to examine the morphology and size of the as-prepared particles. Particle size distributions were obtained from the TEM images by counting several hundreds of particles, using the free software *ImageJ*. Additional information on the size and colloidal stability of the particles in aqueous suspension was obtained from Dynamic Light Scattering (DLS) measurements (Malvern Zetasizer Nano-ZS90). Zeta potential of the particles suspensions was measured in the same equipment. FTIR spectra were recorded in powdered samples diluted in KBr using a JASCO FT/IR-6200 IRT-5000 instrument. The crystalline phase of the particles was characterized by X-ray powder diffraction (XRD) using a Panalytical X'Pert Pro diffractometer (CuKa) with an X-Celerator detector over an angular range of 10º < 2θ < 80º, step width of 0.05º 2θ and 1 second measuring time per step. HighScore Plus software was used to calculate the unit cell parameters of the structure. Refined parameters were background coefficients, scale factor, zero, unit cell parameters and profile parameters. The crystallite size was estimated from the full width at half maximum of the (400) reflection of the $ZnGa_2O_4$ spinel structure (~43.4 °2θ) by using the Scherrer formula. SEM images of the thin films, consisting of $ZnGa_2O_4$:Cr nanoparticles, deposited onto quartz/ZrO_2 substrates, were taken by using a Hitachi S4800 microscope. Film thickness was measured using a benchtop mechanical profilometer (DektakXT Stylus Profiler, Bruker). Radius of the stylus employed was 2 μm and the scanning speed 200 μm·s^{-1}.

2.2.2. Optical characterization of the $ZnGa_2O_4$:Cr films

Ballistic transmittance was measured using a Cary 7000 series UV–vis–NIR spectrophotometer. The excitation and emission spectra of the films were recorded at room temperature using an Edinburgh FLS100 spectroflurometer using emission and excitation wavelengths of 695 nm and 260 nm, respectively. Persistent luminescence decay curves were recorded using the same equipment with the detector at 695 nm. The samples were excited at 260 nm during 10 minutes opening the excitation and emission slits at 13 nm (maximum aperture). To avoid saturation of the detector during the excitation stage, an optical density filter (5%) was placed in the emission pathway. The filter is then quickly removed to record the persistent emission. Thermoluminescence glow curves were recorded by a CCD camera (Princeton Instruments Pixis 100) coupled to a visible monochromator (Acton Spectra Pro, Princeton Instruments, 300 grooves per mm, centered at 700 nm) after prior 5 minutes excitation by a UV lamp (λ_{exc} = 254 nm) at 14 K. In order to minimize the parasitic initial signal from tunneling processes, 30 s delays between the end of the excitation and the beginning of the thermoluminescence measurements were applied.

3. Results and Discussion

3.1. Synthesis and Characterization of the Precursor ZnGa₂O₄:Cr Nanoparticles

Figures 2a and 2b show TEM micrographs of representative particles synthesized with different nominal Cr^{3+} contents (0 to 20%) using acetate and nitrate, respectively, as Zn precursors salts, as described in the experimental section. TEM micrographs of particles synthesized using the whole Cr content range used in this study can be observed in Figure S1. All samples consisted of uniform spherical particles. It should be noticed that the presence of trisodium citrate in the reaction medium was essential to obtain uniform, spherical particles of any Cr composition, including the x= 0 members, as the synthesis in the absence of the organic additive resulted in an ill-defined precipitate in all cases (Figure S2). This behavior may be ascribed to the formation of metal-citrate complexes in solution prior to precipitation, which on heating would give rise to a controlled release of Zn^{2+}, Ga^{3+} and Cr^{3+} cations, thus fulfilling one of the requirements for the formation of uniform particles according to the LaMer and Dinegar model.[40] Likewise, it was important to keep a citrate/Zn molar ratio = 5, as the use of a lower ratio (= 1) produced the precipitation of non-uniform solids (Figure S2) suggesting that under these conditions,

the precipitation rate is too fast due the very small citrate concentration. On the contrary, a higher ratio (= 7) produced no precipitate probably due to the extremely slow decomposition of the citrate complexes.

Figures 2a and 2b reveal that particle diameter drastically changed depending on the Zn precursor and Cr content. Such size variation can be better noticed from Figures S3a and 3b, which present size distributions obtained from the corresponding TEM micrographs of Figure 2. The mean size values obtained from the size distributions of all synthesized samples are listed on Table 1. It can be first observed in this table, that the 0% Cr-containing particles synthesized from Zn nitrate (NZG-0) showed a mean diameter of 300 nm, while the synthesis from Zn acetate rendered 150 nm diameter particles (AZG-0). The size of the particles could therefore be halved by using Zn acetate instead of Zn nitrate as the Zn source. This behavior could be related to the complexing capacity of acetate (higher than that of nitrate),[41] which may slow down the release of Zn^{2+} cations needed for precipitation, thus affecting the nucleation and particle growth kinetics, responsible for final particle size.[40]
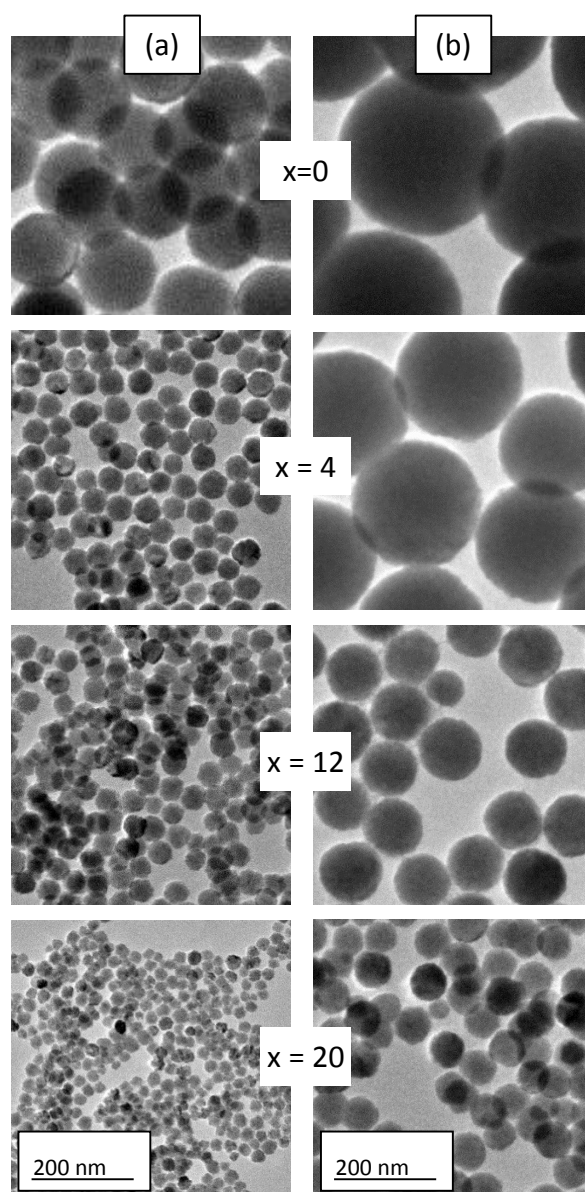
Figure 2: TEM micrographs of the nanoparticles obtained after aging at 200°C for 30 minutes in a microwave oven an aqueous solution containing *a)* $Zn(OAc)_2$ (15 mL, 0.04 M), $Ga(NO_3)_3$ (15 mL, 0.08M), trisodium citrate (30 mL, 0.1M) and the indicated amounts (x) of $Cr(NO_3)_3$ at pH=9 (AZG-x series). *b)* Idem as in a) but using $Zn(NO_3)_2$ as Zn precursor (NZG-x series). The bottom left scale applies to all micrographs.

Table 1 also manifests that when the synthesis was carried out in the presence of increasing nominal amounts of Cr (from 2 to 20%), a decrease in particle diameter clearly occurred in both series of samples (AZG-x and NZG-x), although the NZG-x particles resulted larger than the AZG-x ones for any Cr content, in agreement with the behavior observed for the Cr-free samples. The analysis of the Cr content in the samples by ICP spectrometry (Table 1) confirmed the incorporation of Cr ions to the precipitated particles. These analyses also revealed that the experimental Cr% values were, in all cases, significantly lower than the nominal Cr contents added to the starting solutions.

This fact could be due to the higher stability of the Cr^{3+}-citrate complex[42] compared to
those of the Zn^{2+}-citrate[43] and Ga^{3+}-citrate[44] ones, which must preclude the complete decomposition of the former. Chromium ions in excess remain in solution after the nanoparticles precipitation, and they are removed by washing.

Table 1: Mean particle diameter measured on TEM micrographs, ICP analysis of Cr content, Zeta potential values of aqueous suspensions at pH= 10, and unit cell parameter of $ZnGa_2O_4$ spinel phase of the $ZnGa_2O_4:Cr^{3+}$ particles synthesized from Zn acetate (AZG-x series) and Zn nitrate (NZG-x series).

| x (Nomin. mol% Cr)	TEM size (nm)		ICP (mol% Cr^{3+})		Zeta potential (mV)		Unit cell parameter (Å)	
	AZG-x	NZG-x	AZG-x	NZG-x	AZG-x	NZG-x	AZG-x	NZG-x
0	150(8)	294(26)	0	0	-36.8	-54.5	8.3825 (8)	8.3816(8)
2	50(6)	269(20)	0.09	0.03	-35.2	-45.8	8.3754 (9)	8.3767(8)
4	53(5)	243(15)	0.13	0.06	-28.0	-47.5	8.3638 (8)	8.3756(8)
6	43(4)	213(13)	0.25	0.11	-31.0	-40.6	8.3646 (8)	8.3741(8)
8	40(4)	189(8)	0.29	0.21	-33.3	-27.3	8.3615 (9)	8.3714(8)
12	29(3)	131(6)	0.58	0.27	-45.1	-41.8	8.3604(9)	8.3658(8)
20	27(3)	95(5)	0.99	0.59	-41.8	-41.0	8.3566 (9)	8.3584(9)
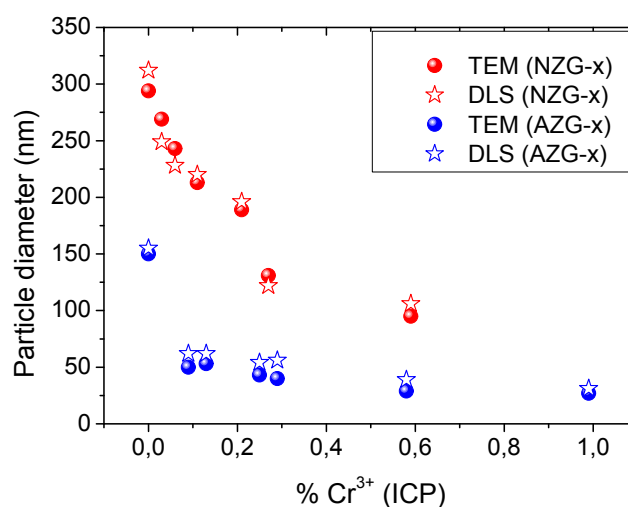
Figure 3: Particle diameter values calculated from TEM micrographs and from DLS measurements versus experimental Cr content (ICP) of NZG-x and AZG-x particles.

Figure 3 shows the size evolution with the experimental Cr content for both series of samples. It can be observed that the decrease of particle size with Cr content was gradual (from 300 nm down to 100 nm) for the NZG-x samples. However, a striking reduction in size was observed for very small amounts of Cr (from 150 nm down to 50 nm) followed by a further slight decrease in size with Cr content (from 50 nm to 30 nm) in AZG-x particles. It should be noted that for nominal amounts of Cr^{3+} above 20% (experimental Cr^{3+} contents above x=0.99 and x=0.59 for the AZG and NZG series, respectively), irregular particles not suitable for our purpose, were obtained. These effects of Cr^{3+}

doping on the size of the particles could be due to the influence of doping cations on the precipitation energy barriers, and therefore, on the kinetics of the nucleation and particles growth, which determine the final particles size and shape, according to the LaMer and Dinnegar model.[45] It is worth noting that the effect of tuning particle size with varying doping ion concentration has been observed before in systems doped with lanthanide ions[46,47]. This is the first time that Cr content is proposed as a tool to tune $ZnGa_2O_4$:Cr particle size.

This is the first report on the effect of Cr^{3+} doping content on the size of the synthesized nanoparticles. This relevant result allows designing $ZnGa_2O_4$:Cr particles on demand in the 30 nm – 300 nm diameter interval.

The mean hydrodynamic size obtained by means of DLS measurements in aqueous suspensions of the particles (pH =10) is shown in Figure 3. It can be observed that the values obtained were, in all cases, very similar to the values measured on the TEM micrographs, thus demonstrating that the particles were well dispersed in such aqueous suspensions. This behavior can be justified in view of the high values of the zeta potential measured for all suspensions (Table 1), which should give rise to a high repulsive interaction between the colloidal nanospheres. Such a high value of Z potential must be associated with the presence of citrate anions adsorbed on the nanoparticles surface, which is revealed by FTIR spectroscopy. Thus, the FTIR spectra of the AZG-4 and NZG-4 samples (Figure S4) chosen, as a representative example, were very similar to each other showing bands at 3435 cm^{-1} and 1630 cm^{-1}, associated to absorbed water molecules, at 602 cm^{-1} and 427 cm^{-1} that correspond to the characteristic Zn-O and Ga-O vibrations of the $ZnGa_2O_4$ spinel matrix[48] and at 1590 cm^{-1} (overlapped with that of water) and 1400 cm^{-1}. The latter are characteristic of carboxylic groups in sodium citrate as indicated by the spectrum of pure sodium citrate also shown in Figure S4 with comparative purposes.

The crystalline structure of the particles was identified by XRD (Figures 4a and 4b). All diagrams were very similar to each other and showed, exclusively, reflections corresponding to the $ZnGa_2O_4$ spinel cubic phase (PDF ICDD 00-038-1240). The unit cell parameters exhibited a slight and progressive decrease with increasing Cr content for both series of samples (Table 1) indicating the isomorphic substitution of smaller Cr^{3+} (ionic radius in VI coordination = 0.615 Å) for slightly bigger Ga^{3+} (ionic radius in VI coordination = 0.620 Å) in the $ZnGa_2O_4$ unit cell. To get an idea about the single or polycrystalline character of the synthesized particles, we have estimated the crystallite

size by applying the Scherrer formula to the (400) reflection located at ~43.3° 2θ. The values obtained were plotted, as a function of Cr content, in Figure 4c and compared with the particle diameter as measured on the TEM micrographs. Only crystallite sizes corresponding to the AZG series could be calculated, as those of the NZG samples were all higher than 100 nm, which hindered the application of Scherrer formula. It can be observed that the values of the crystallite size and particle diameter were practically the same for all Cr-containing samples, which suggests that the particles were single crystals.
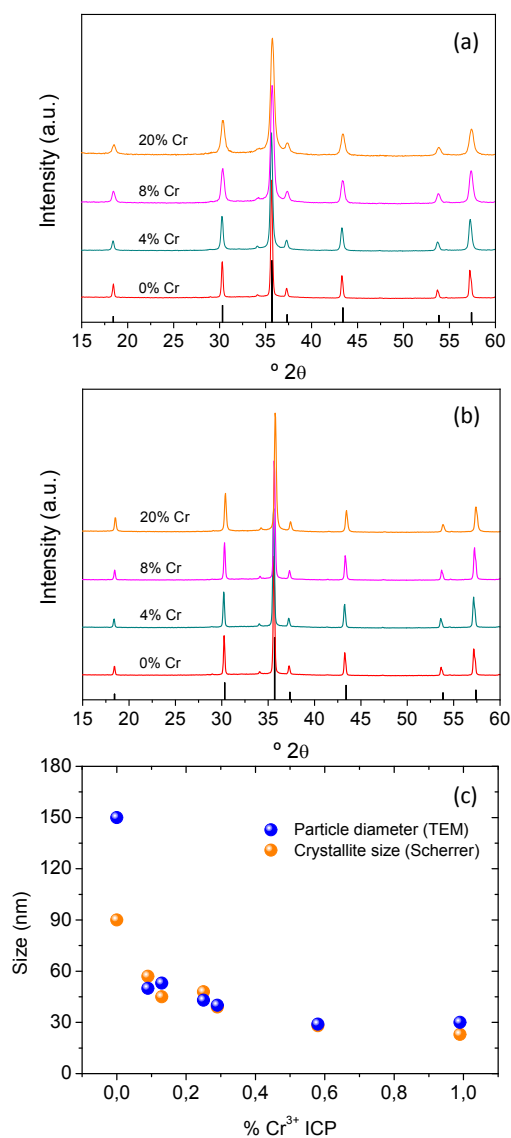

Figure 4: XRD patterns of AZG-x (a) and NZG-x (b) particles with different nominal Cr contents. Reflections at the bottom of each graph correspond to cubic $ZnGa_2O_4$ spinel (PDF ICDD 00-038-1240). c) Particle diameter measured on TEM micrographs and crystallite size calculate using Scherrer formula versus Cr content for AZG-x particles.

In fact, the HREM image corresponding to an individual AZG-2 nanoparticle shown in Figure 5, showed as a representative example, exhibited bright fringes extending all across the nanoparticle, which reinforced this result. Their d spacing (4.9 Å) corresponds

to the (111) planes of the $ZnGa_2O_4$ spinel structure. The sample synthesized in the absence of Cr^{3+} showed, however, a Scherrer crystallite size (90 nm) clearly lower than the corresponding particle diameter measured on the TEM micrograph (150 nm). However, it should be noticed that the high crystallite size obtained in this case, close to 100 nm, could be too high to be reliable as calculated by using the *Scherrer* equation and cannot be used to get information about the single or polycrystalline character of these particles.
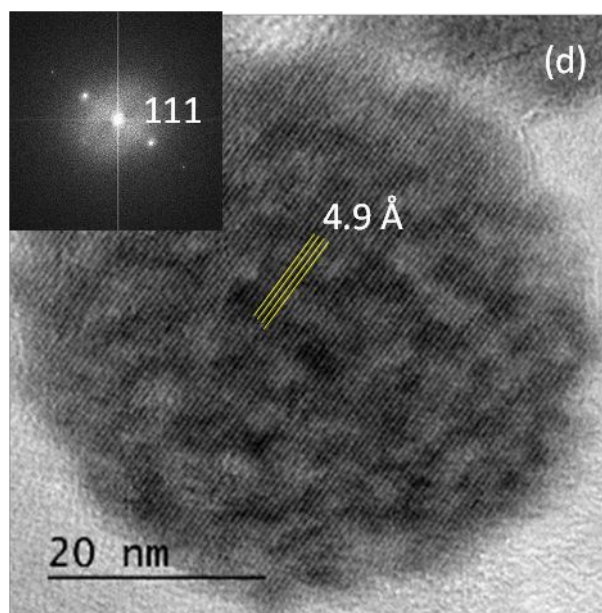

Figure 5: HREM micrograph showing bright fringes across a AZG-2 nanoparticle. The inset is an indexed DDP calculated from the whole particle.

In summary, while previous authors used time- and energy consuming methods that do not provide full control over size, shape, uniformity or dispersibility of $ZnGa_2O_4$:Cr nanoparticles, our approach allows a fine control of all these parameters, which is relevant for applications ranging from bioimaging, biolabeling or chemical sensing to signaling or energy harvesting nanosized devices. Following is the description of a nanodevice showing red to NIR persistent emission consisting in a transparent thin film fabricated from the nanoparticles suspensions shown above.

3.2. Preparation and Characterization of the $ZnGa_2O_4$:Cr Thin Films

Although any of the nanoparticles synthesized above could be used to prepare uniform thin films, it is important to keep the size into the nanometer range (≤ 100 nm) to minimize light scattering and maximize transparency. Based on this premise, the AZG-12 and NZG-20 samples, showing nanoparticles with diameters close to 30 nm and 100 nm,

respectively were selected as precursors to prepare nanophosphors thin films. The selection of both samples obeyed to two additional reasons. On the one hand, they represent the two size extremes within nanometer range and can be used, therefore, to analyze the influence, if any, of the precursor particles size on the optical properties of the films. On the other hand, their very similar experimental Cr contents (0.58% and 0.59%, respectively) further allowed comparing the luminescent properties of the corresponding films independently of such parameter.

The films were prepared by spin coating from suspensions of the nanoparticles in methanol on quartz/ZrO_2 substrates, as described in the experimental section. Films prepared from the 30 nm nanoparticles will be called 30F films while those fabricated from 100 nm nanoparticles will be named 100F films. In general, nanophosphors show an intrinsically low emission intensity as a consequence of their large surface to volume ratio and the subsequent high number of surface quenchers (citrate and OH groups in our case, as inferred from the FTIR spectra).[49] In order to improve such emission intensity, the films were calcined at 500 ºC and 900 ºC for 12 hours. Calcination at high temperature is also expected to improve the persistent luminescence,[16,17,21] as confirmed further in this paper. Plane-view SEM images, all of them taken at the same magnification, of both 30F and 100F films, as-prepared and after annealing at 500 ºC and 900 ºC, are displayed in Figure 6, left. It can be observed that the uniform shape and size of the precursor nanoparticles allowed full coverage of the substrate after the spin coating process with both nanoparticles suspensions and that such coverage was kept intact after the annealing processes. The shape and size of the nanoparticles did not essentially changed after annealing at 500 ºC for any of the films, whereas they suffered a significant sintering degree when the films were annealed at 900 ºC, which was more evident for that obtained for the smallest particles (AZG-12). The SEM micrographs show that such sintering process increased the grain size of both films, although the particles of the 100F film were still larger than those of the 30F one. Finally, annealing at 900 ºC also gave rise to a shape transformation from spherical to polygonal, especially obvious in the particles of the 100F film. On the other hand, the cross sections of the as prepared films were uniform (Figure 6, right), with thicknesses of 371 nm and 247 nm for the 30F and 100 F films, respectively. The thickness of both films decreased after calcination due to densification, as shown in Table 2, although the shrinkage of the 30F films was more significant than that of the 100F films due to the size of the packing particles. Table 2 also shows the data

corresponding to the thickness values of all films measured with the profilometer, which matched well those obtained from the SEM images, thus demonstrating again the uniformity of the films.
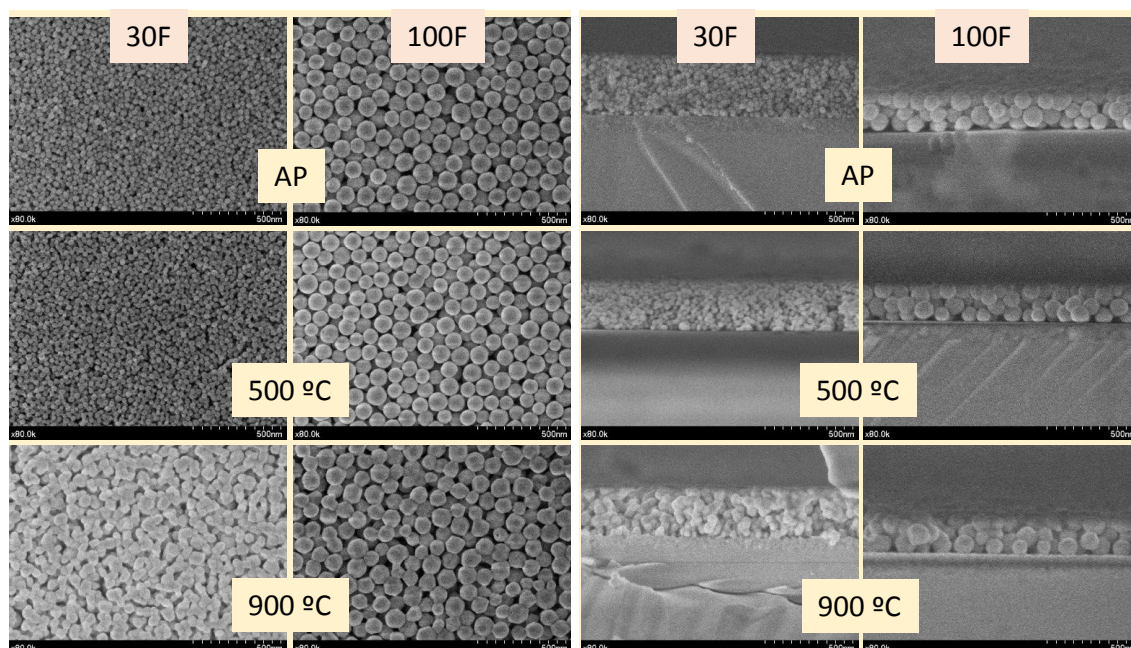
Figure 6: Front views (left) and cross sections (right) of thin films, deposited over ZrO_2 coated quartz substrates by spin coating from 30 nm (30F films) and 100 nm (100F films) $ZnGa_2O_4$:Cr^{3+} nanoparticles, as prepared (AP) and after calcination at 500 ºC and 900 ºC for 12 h.

Table 2: Thickness values of the $ZnGa_2O_4$:Cr^{3+} films, before and after calcination, obtained from SEM cross sections and from profilometry.

	30F films		100F films	
	SEM (nm)	Profilometer (nm)	SEM (nm)	Profilometer (nm)
AP	371±3	358.0±1.9	247±1	246.29±2.6
500 ºC	306±3	311.6±8.0	227±1	229.9±9.6
900 ºC	279±5	264.4±12.8	227±2	226.6±10.7

3.3 *Optical Properties of the ZnGa₂O₄:Cr Thin Films*

The transparency of the as-prepared films and of the films after annealing has been spectroscopically analyzed by recording their ballistic transmittance (T_B, defined as the fraction of the incident light transmitted in the incoming direction). The T_B curve of a quartz/ZrO_2 substrate was also recorded as a reference (Figures 7a and 7b). In general, the curves of the quartz/ZrO_2 and the films before and after annealing at 500 ºC were very similar to each other, while those of the films annealed at 900 ºC showed lower T_B values. These values were however all well above 80% for any wavelength analyzed, which

suggests the high optical quality even of the layers processed at the highest annealing temperature. It should be noted that the Cr^{3+} absorption, expected at 415 nm and 550 nm as explained below, cannot be seen on Figures 7a and 7b, due to small Cr content, small oscillator strengths and small thickness.
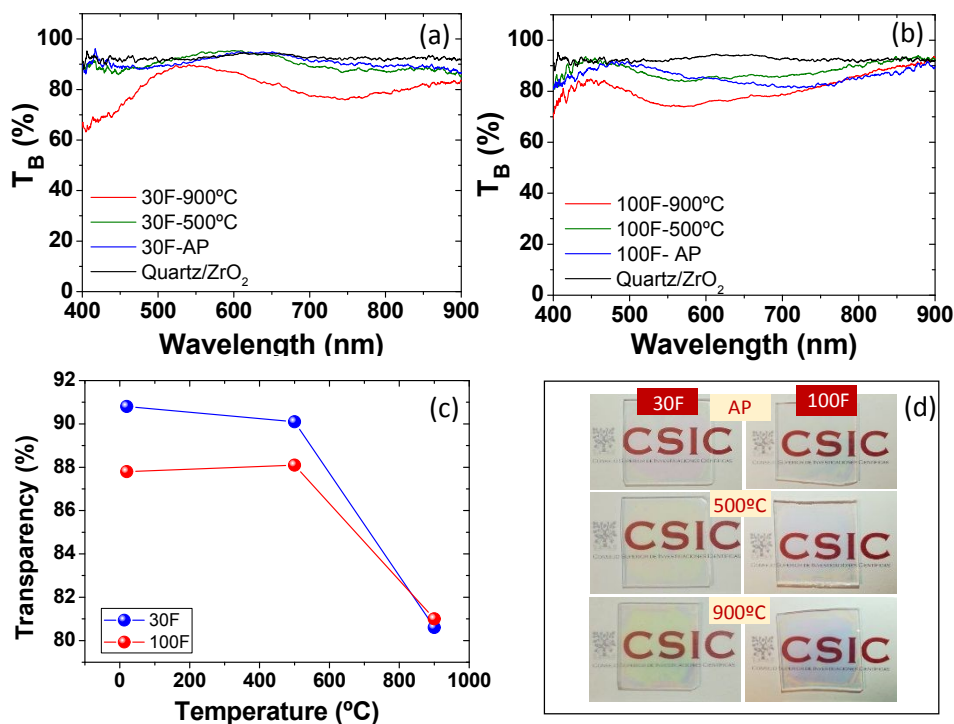

Figure 7: Spectral dependence of the ballistic transmittance (T_B) of 30F (a) and 100F (b) $ZnGa_2O_4$:Cr^{3+} thin films as-prepared (AP) and after calcination at 500 ºC and 900 ºC for 12 hours. The T_B for a quartz/ZrO_2 substrate is also shown. c) Annealing temperature dependence of the transparency of the films. Lines are guides to the eye. d) Digital pictures of light reflected under daylight from the films placed over a white paper with the CSIC logo.

The transparency of the films has been quantified from the area under the curve ($\int_{400}^{750} T_B(\lambda)d\lambda$) of the spectra shown in Figures 7a and 7b and given in Figure 7c as a function of temperature. The transparency value of a hundred percent corresponds to a medium through which light goes through without any scattering. It can be observed that the as-prepared films and those annealed at 500 ºC show very high and constant transparency values (close to 90%), the 30F films showing slightly higher values than the 100F ones. Annealing at 900ºC causes a drop in the transparency value of both films to about 80%. This is likely due to the larger size of the particles observed after the annealing process, which increase the scattering strength of the films and consequently lessen T_B. However, the T_B values obtained are still high enough as to confer both films with a high optical quality, as demonstrated in the digital camera pictures shown in Figure 7d.
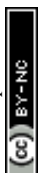
Figure 8a shows the photoluminescence excitation spectra corresponding to the emission at 695 nm recorded on the 30F and 100F films before and after annealing at 500 ºC and 900 ºC. They all show an intense band centered at around 250 nm while two much weaker bands can be observed at ~410 nm and ~555 nm in the films annealed at 900 ºC. According to the literature, the strong band results from the transition from the valence band to the conduction band of the host whereas the weak bands in the visible range correspond to $^4A_2(^4F) \rightarrow ^4T_1(^4F)$ and $^4A_2(^4F) \rightarrow ^4T_2(^4F)$ electronic transitions between energy levels splitted by the crystal field strength.[3] The excitation band due to the third characteristic transition of Cr^{3+} ions ($^4A_2(^4F) \rightarrow ^4T_1(^4P)$), expected at about 290 nm,[3] overlaps with the band-to-band absorption and is therefore not observed. The emission spectra recorded under excitation at 250 nm of the as-prepared 30F and 100F films and after annealing at 500 ºC and 900 ºC are shown in Figure 8b. The spectra indicated, in general, a progressive increase in emission intensity with increasing annealing temperature. The calcined 100F films showed, in addition, higher emission intensity than the 30F films processed at the same temperature, in spite of the higher thickness of the latter. This result could be due to the larger grain size of the former, as described above, which decrease the grain boundary that usually act as non-radiative recombination centers, enhancing the photoluminescence intensity.[38]

On the other hand, while the spectra of the as-prepared films and those of the films calcined at 500 ºC just showed two broad unresolved bands, those of the films calcined at 900 ºC exhibited a well-defined structure as a consequence of the improved crystallinity revealed by the increased grain size shown in Figure 6. Two emission lines of different origins can be distinguished in the spectral structure, namely R and N2, labeled in the Figure, which are in good agreement with the literature.[16] The emission at 688 nm (R line) is known as the zero phonon line of the $^2E(^2G) \rightarrow ^4A_2(^4F)$ transition of Cr^{3+} in an octahedral crystal field (Ga^{3+} site). The R line exhibits Stokes Phonon Side Bands (PSB) at 708 nm, 715 nm and 722 nm and Anti-Stokes PSB at 670 nm and 680 nm. The second line, N2 line, located at 695 nm, originates from another type of Cr^{3+} ion relative to the ideal octahedral coordination of the normal spinel, and is associated with Cr^{3+} ions possessing a neighboring antisite defect pair ($Ga_{Zn}°$ and Zn_{Ga}'). This type of Cr^{3+} ion plays a specific role in the long-lasting luminescence process.[17]
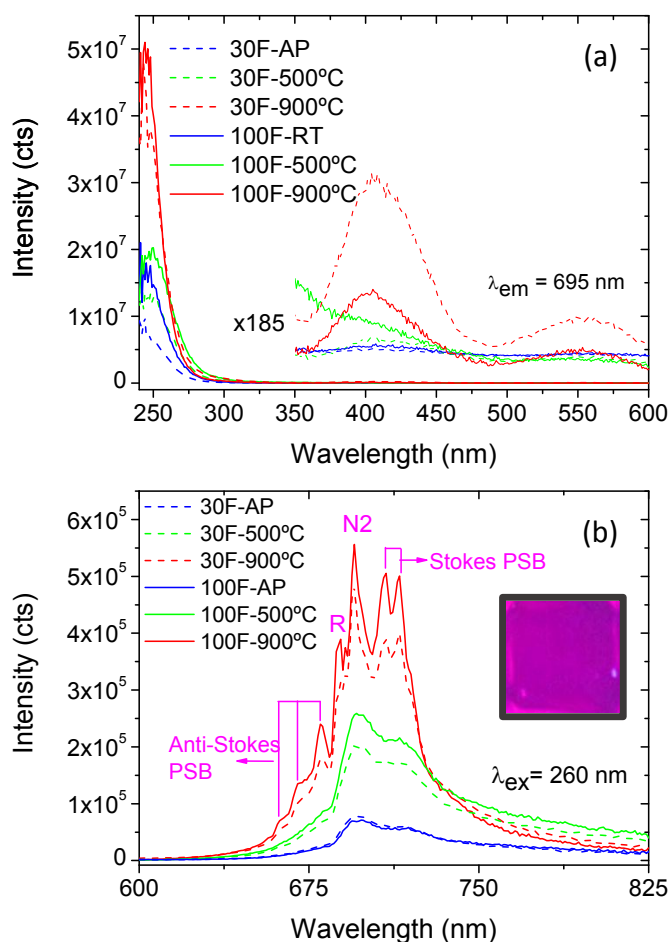
Figure 8: Excitation (a) and emission (b) photoluminescence spectra of 30F and 100F $ZnGa_2O_4:Cr^{3+}$ thin films as-prepared (AP) and after calcination at 500 ºC and 900 ºC for 12 hours. The inset in (b) is a photograph of the 100F-900ºC film under UV excitation.

The persistence luminescence decay curves of the 30F and 100F films, before and after annealing at 500 ºC and 900 ºC, were therefore monitored at 695 nm, the films being previously excited at 260 nm for 5 min (Figures 9a and 9b). A wavelength of 695 nm was selected for this experiment because this light originates from Cr^{3+} ions possessing a neighboring anti-site defect pair, which plays an important role in the long-lasting luminescence process, as commented above.

Both 30F and 100F films, at each processing temperature, showed persistent luminescence decays recordable for more than 1000 s and they exhibited similar decay slopes. On the other hand, the persistent luminescence intensities significantly varied from one film to another. Indeed, likewise photoluminescence intensity, the persistent luminescence intensity of both 30F and 100F increases with calcination temperature. Two effects brought by the increase of the calcination temperature can be linked to this

observation: *(i)* the elimination of surface quenchers, such as citrate ions absorbed on the nanoparticles surface and *(ii)* the crystallinity improvement, as inferred from photoluminescence measurements, leading to a higher concentration of efficient traps for persistent luminescence at room temperature. As a result, the persistent luminescence can be recorded for longer times with the films annealed at 900 °C.

Although longer persistence has been reported for bulk $ZnGa_2O_4$:Cr powders by other authors,[33,34] comparison with the persistence measured on our films is meaningless as we are irradiating a very small area of a really thin film (~300 nm) by focusing a xenon lamp, while, in the referenced papers, the authors irradiated a very large area of a powder sample with a UV lamp. In addition, the time duration of the luminescence always depends on the real performance of applied apparatus, as emphasized by Xu and Tanabe.[1]

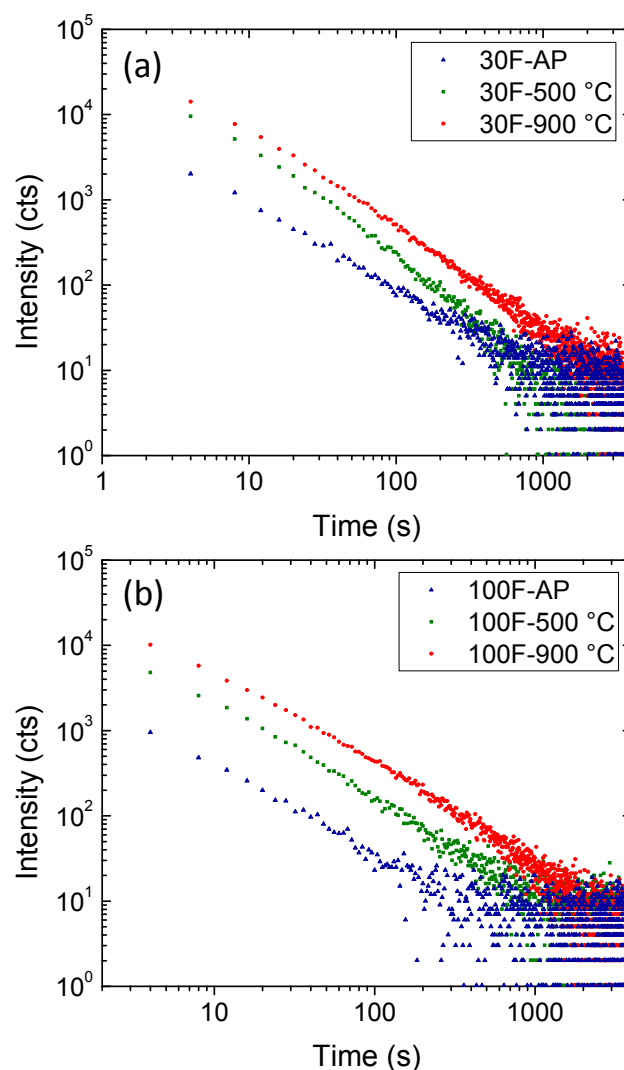**Figure 9:** Persistent luminescence decay curves of 30F (a) and 100F (b) ZnGa$_2$O$_4$:Cr^{3+} thin films as-prepared (AP) and after calcination at 500 ºC and 900 ºC for 12 hours recorded after 10 minutes excitation at 260 nm.

Thermally stimulated luminescence (TSL) is a powerful tool to investigate the depths and distribution of the traps present in persistent luminescence phosphors. The material is first excited using suitable wavelength at low temperature (254 nm at 14 K and 5 min in our case) to stimulate charge trapping (electrons and holes). The phosphor is then heated at a constant rate (10 K·min^{-1}) while the TSL signal is recorded. When the thermal energy is sufficient, the trapped charges are released and give rise to the emission of photons. The maximum temperature of the TSL peaks can be related to the trap depth while the peak width provides information on the trap-depth distribution, which is somehow related to the structural disorder of the material.[50] Figure 10 shows the TSL glow curves obtained for the 30F and 100F films. The as-prepared films showed no significant TSL, while TSL signals extending over a broad temperature range, were observed for both films annealed

at 500 ºC and 900 ºC, indicating a broad trap distribution arising from multiple defects. The important broadness of the TSL glow curves around the working temperature (*i. e.* room temperature in our case) may explain the similar slopes of the persistent luminescence decays previously observed (Figure 9). Interestingly, the TSL glow curves sharpened and shifted towards higher temperature while increasing the calcination temperature. Therefore, the shallow traps, that may be related to surface defects were minimized at high temperature while the deeper traps, that are the signature of antisite defect pairs were stabilized with the calcination temperature as a result of the crystallinity improvement. This is in perfect agreement with previous studies of the crystallization temperature effect on the persistent luminescence properties of $ZnGa_2O_4$:Cr^{3+} nanoparticles embedded in glass.[53] Subsequently, the maximum of the TSL glow peak is slightly higher than the working temperature for the 900 °C calcined films and therefore gets closer to the optimum temperature compared to 500 °C annealed films.[51] This is in good agreement with the improved persistent luminescence decays obtained for the 900 °C calcined films compared to the 500 °C ones.
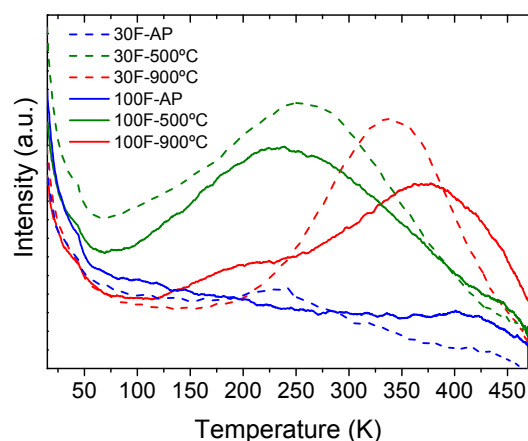

Figure 10: TSL curves recorded after excitation at 254 nm for 5 min and 14 K of 30F and 100F $ZnGa_2O_4$:Cr^{3+} thin films as-prepared (AP) and after calcination at 500 ºC and 900 ºC for 12 hours.

The trap depth energies were estimated from the maxima of the TSL curves (T_M) using the Randal and Wilkins formula ($E_{traps}=T_M/500$)[52] and listed in Table 3. The values obtained for the films annealed at 900 ºC are in agreement with those reported in the literature for $ZnGa_2O_4$:Cr powders annealed at similar temperatures.[53,54,55] Trap depths in

the ~0.5−1 eV range, as is the case of our films, enable a progressive release of carriers at room temperature, giving rise to persistent luminescence, as observed here.

Table 3: Peak maxima of the Cr^{3+} thermoluminescence glow curves shown in Figure 10 and corresponding trap depths.

	30F		100F	
	T_M (K)	E_{traps} (eV)	T_M (K)	E_{traps} (eV)
500 ºC	260	0.52	250	0.50
900 ºC	340	0.68	370	0.74

4. Conclusions

Firstly, a quick synthesis method has been developed which allows the synthesis of uniform, well dispersed $ZnGa_2O_4$:Cr^{3+} spherical particles with tunable diameter in the 30 nm − 300 nm range. Second, two different transparent thin films have been fabricated by spin coating using 30 nm and 100 nm $ZnGa_2O_4$:Cr^{3+} nanoparticles suspensions to investigate the effect of particle size on luminescence. A post annealing of the films at high temperature (900ºC) allowed increasing the emission intensity and the afterglow time of the nanophosphors films by around one order of magnitude while preserving their transparency and uniformity. Although the annealed films made from the 100 nm nanoparticles showed higher photoluminescence emission intensity and deeper traps depth, the persistence of luminescence was found to be independent of the size of the precursor nanoparticles. In summary, a global strategy is presented in this work to construct highly uniform, transparent thin films with red to NIR persistent emission, from colloidal suspensions of different size $ZnGa_2O_4$:Cr^{3+} nanoparticles for the first time in literature. This approach is shown to be a promising route for the fabrication of spinel-based transparent thin films with persistent luminescence as it is an economic and simple technique compared to traditionally used magnetron sputtering methods. The so prepared films may have great potential application in the fields of chemical sensing, information storage, safety signs, and anticounterfeit technology.

Electronic supplementary information

TEM images of all members of the nanoparticles series AZG-x and NZG-x, TEM micrographs of precipitates obtained in the absence of citrate, histograms showing size distributions of particles in Figure 2 of the manuscript, FTIR spectra of NZG-4 and AZG-4 particles.

Authors contributions

Investigation: E.A, B.M. and V.C.; Supervision: M.O., G.L. and A.I.B.; Funding acquisition: M.O., G.L. and A.I.B.; Writing − original draft and Visualization: A.I.B.; Writing − review & editing: M.O. and G.L.

Conflicts of interest

There are no conflicts to declare.

Acknowledgements

REFERENCES

1 J. Xu, S. Tanabe, *J. Lumin.* 2019, **205**, 581−620.

2 Y. Li, M. Gecevicius, J. Qiu, *Chem. Soc. Rev.* 2016, **45,** 2090−2136.

3 T. Maldiney, A. Bessière, J. Seguin, E. Teston, S.K. Sharma, B. Viana, A. J. J. Bos, P. Dorenbos, M. Bessodes, D. Gourier, D.Scherman, C. Richard, *Nat. Mater.* 2014, **13,** 418−426.

4 R. Gao, D. Yan, *Chem. Comm.* 2017, **53,** 5408−5411.

5 L. Wang, Y. Lv, T. L. Zhou, R. J. Xie, Y. Zhuang, *Adv. Func. Mater.* 2018, **28,** p.1705769.

6 P. F. Smet, D. Poelman, M. P. Hehlen, *Opt. Mater. Express* 2012, **2**, 452–454.

7 K. Jiang, L. Zhang, J. F. Lu, C. X. Xu, C. Z. Cai, H. W. Lin, *Angew. Chem., Int. Ed.* 2016, **55,** 7231–7235.

8 N. Gan, H. Shi, Z. An, W. Huang, *Adv. Funct. Mater.* 2018, **28,** 1802657.

9 X. Yang, D. Yan, *Adv. Opt. Mater.* 2016, **4,** 897−905.

10 K. Jiang, L. Zhang, J. Lu, C. Xu, C. Cai, H. Lin, *Angew. Chem., Int. Ed.* 2016, **55,** 7231−7235.

11 L. Wang, Z. Shang, M. Shi, P. Cao, B. Yang, J. Zou, *RSC Adv.*, 2020, **10,** 11418−11425.

12 H. C. Swart, J. J. Terblans, O. M. Ntwaeaborwa, R. E. Kroon, B. M. Mothudi, *Physica B* 2012, **407**, 1664–1667.

Journal of Materials Chemistry C Accepted Manuscript

13 E. Karacaoglu, E. Öztürk, M. Uyaner, M. D. Losego, *J. Amer. Ceram. Soc.* 2020, **103,** 3706−3715.

14 C. Chen, H. Li, J. Jin, X. Chen, Y. Cheng, Y. Zheng, D. Liu, L. Xu, H. Song, Q. Dai, *Adv. Energy Mater.* 2017, **7,** 1700758.

15 P. D. Nsimama, O.M. Ntwaeaborwa, H. C. Swart, *J. Lumin.* 2011, **131**, 119−125.

16 A. Bessière, S. Jacquart, K. Priolkar, A. Lecointre, B. Viana, D. Gourier, *Opt. Express*, 2011, **19,** 10131−10137.

17 A. Bessière, S. K. Sharma, N. Basavaraju, K. R. Priolkar, L. Binet, B. Viana, A. J. J. Bos, T. Maldiney, C. Richard, D. Scherman, D. Gourier, *Chem. Mater.* 2014, **26,** 1365−1373.

18 A. De Vos, K. Lejaeghere, D. E. P. Vanpoucke, J. J. Joos, P. F. Smet, K. Hemelsoet, *Inorg. Chem.* 2016, **55,** 2402−2412.

19 N. Basavaraju, K. R. Priolkar, D. Gourier, S. K. Sharma, A. Bessière, B. Viana, *Phys. Chem. Chem. Phys.*, 2015, **17,** 1790−1799.

20 M. Allix, S. Chenu, F. Véron, T. Poumeyrol, E. A. Kouadri-Boudjelthia, S. Alahraché, F. Porcher, D. Massiot, F. Fayon, *Chem. Mater.* 2013, **25,** 1600−1606.

21 J. Nie, Y. Li, S. Liu, Q. Chen, Q. Xu, J. Qiu, *Sci. Rep.* 2017, **7,** 12392.

22 J. Su, S. Ye, X. Yi, F. Q. Lu, X. B. Yang, Q. Y. Zhang, *Opt. Mater. Express* 2017, **7,** 734−743.

23 Z. Pan, V. Castaing, L. Yan, L. Zhang, C. Zhang, K. Shao, Y. Zheng, C. Duan, J. Liu, C. Richard, B. Viana, *J. Phys. Chem. C*, 2020, **124,** 8347–8358.

24 W. Zhang, J. Zhang, Y. Li, Z. Chen, T. Wang, *Appl. Surf. Sci.* 2010, **256**, 4702–4707.

25 H. W. Choi, B. J. Hong, S. K. Lee, K. H. Kim, Y. S. Park, *J. Lumin.* 2007, **126,** 359–364.

26 O. M. Bordun, V G. Bihday, I. Y. Kukharskyy, *J. Appl. Spectr.*, 2014, **81,** 43–48.

27 Q. Shi, C. Wang, D. Zhang, S. Li, L. Zhang, W. Wang, J. Zhang, *Thin Solid Films* 2012, **520,** 6845–6849.

28 C. S. Kamal, S. Boddu, B. Vishwanadh, K. R. Rao, V. Sudarsan, R.K. Vatsa, *J. Lumin.* 2017, **188,** 429–435.

29 S. Chenu, E. Véron, C. Genevois, A. Garcia, G. Matzen, M. Allix, *J. Mater. Chem. C*, 2014, **2**, 10002-10010.

30 V. Castaing, A. D. Sontakke, J. Xu, A. J. Fernández-Carrión, C. Genevois, S. Tanabe, M. Allix, B. Viana, *Phys. Chem. Chem. Phys.,* 2019, **21**, 19458.

31 D. Geng, G. Lozano, H. Miguez, *ACS Appl. Mater. & Int.* 2019, **11,** 4219–4225.

32 Z. Li, Y. Zhang, X. Wu, L. Huang, D. Li, W. Fan, G. Han, *J. Am. Chem. Soc.* 2015, **137,** 5304–5307.

33 T. Ai, W. Shang, H. Yan, C. Zeng, K. Wang, Y. Gao, T. Guan, C. Fang, J. Tian, *Biomaterials* 2018, **167,** 216−225.

34 Y. Wang, C. X. Yangn, X. P. Yan, *Nanoscale*, 2017, **9,** 9049−9055.

35 H. Liu, F. Ren, H. Zhang, Y. Han, H. Qin, J. Zeng, Y. Wang, Q. Sun, Z. Li, M. Gao, *J. Mater. Chem. B*, 2018, **6,** 1508−1518.

36 E. Teston, S. Richard, T. Maldiney, N. Liavre, G. Y. Wang, L. Motte, C. Richard, Y. Lalatonne, *Chem. Eur. J.* 2015, **21,** 7350–7354.

37 M. Sun, D. Li, W. Zhang, Z. Chen, H. Huang, W. Li, Y. He, X. Fu. J. Solid State Chem. 2012, 190, 135–142.

38 D. Geng, G. Lozano, M. E. Calvo, N. O. Núñez, A. I. Becerro, M. Ocaña, H. Míguez. *Adv. Optical Mater.* 2017, **5,** 1700099.

39 A. Zelcer, G. J. A. A. Soler-Illia, *J. Mater. Chem. C* 2013, **1,** 1359−1367.

Journal of Materials Chemistry C Accepted Manuscript

Journal of Materials Chemistry C Accepted Manuscript

40 V. LaMer, R. Dinegar, *J. Am. Chem. Soc.* 1950, **72,** 4847−4854.

41 R. Díaz-Torres, S. Alvar, *Dalton Trans.* 2011, **40,** 10742–10750.

42 C. Gabriel, C. P. Raptopoulou, A. Terzis, V. Tangoulis, C. Mateescu, A. Salifoglou, *Inorg. Chem.* 2007, **46,** 2998–3009.

43 S. Capone, A. Robertis, C. Stefano, S. Sammartano, *Talanta* 1986, **33,** 763–767.

44 M. Matzapetakis, M. Kourgiantakis, M. Dakanali, A. Salifoglou, C. P. Raptopoulou, A. Terzis, A. Lakatos, T. Kiss, I. Banyai, L. Iordanidis, T. Mavromoustakos, *Inorg. Chem.* 2001, **40,** 1734–1744.

45 V. LaMer, R. Dinegar, *J. Am. Chem. Soc.* 1950, **72**, 4847–4854.

46 D. Chen, Y, Wang, *Nanoscale*, 2013, **5**, 4621–4637.

47 A. I. Becerro, M. Ocaña, *RSC Adv.*, 2015, **5**, 34517–34524.

48 P. M. Aneesh, K. M. Krishna, M. K. Jayaraj, *J. Electrochem. Soc.* 2009, **156,** 33–36.

49 N. O. Nuñez, S. Rivera, D. Alcantara, J. M. de la Fuente, J. Garcia-Sevillano, M. Ocaña. *Dalton Trans.* 2013, **42,** 10725−10734.

50 M. Martini, F. Meinardi, *Rivista del nuovo Cimento*, 1997, **20,** 1−71.

51 J. Du, O. Q. De Clerq, D. Poelman, *Sci. Rep.*, 2019, **9**, 10517.

52 J. T. Randall, M. H. F. Wilkins, *Proc. R. Soc. London, Ser. A* 1945, **184,** 365−389.

53 V. Castaing, A. D. Sontakke, A. J. Fernandez-Carrion, N. Touati, L. Binet, M. Allix, D. Gourier, B. Viana, *Eur. J. Inorg. Chem.* 2017, 5114−5120.

54 S. K. Sharma, D. Gourier, E. Teston, D. Scherman, C. Richard, B. Viana, *Opt. Mater.* 2017, **63,** 51−58

55 L. Song, P. P. Li, W. Yang, X. Hui Lin, H. Liang, X. F. Chen, G. Liu, J. Li, H. H. Yang, *Adv. Funct. Mater.* 2018, **28,** 1707496.